Microstructure evolution of a W-doped ZrB_2 composite upon high-temperature oxidation

Laura Silvestroni[1*], Diletta Sciti[1], Frédéric Monteverde[1], Kerstin Stricker[2], Hans-Joachim Kleebe[2]

[1]*CNR-ISTEC, National Research Council of Italy - Institute of Science and Technology for Ceramics, Via Granarolo 64, I-48018 Faenza (RA), Italy*

[2]*TU-IAG, Technische Universität Darmstadt - Institut für Angewandte Geowissenschaften, Schnittspahnstraße 9, 64287 Darmstadt, Germany*

ABSTRACT

This basic research deals with the microstructure evolution of a W-doped ZrB_2 composite, from the as-sintered aspect and upon oxidation at 1650°C. In the pristine material, the original ZrB_2 nuclei are surrounded by a mixed $(Zr,W)B_2$ solid solution, refractory W-compounds are found at triple junctions and clean grain boundaries are distinctive of this ceramic. After oxidation, a novel microstructure forms and is typified by an intragranular nanostructure, in which nanosized W particles are located within the ZrO_2 columnar grains. Combined microstructure analysis and thermodynamics computation enable to shed light on the emblazoned role of W in ZrB_2 compounds.

Keywords: ZrB_2, W-compounds, transmission electron microscopy, high temperature oxidation.

1. Introduction

Zirconium diboride is one of the most investigated compounds in the ultra-high temperature ceramics (UHTCs) class of materials, thanks to its unique combination of chemical and structural properties and its potential employ in space and energy production sectors [1].

Recent research activities in structural applications of ZrB_2-based composites pointed out that the addition of W-bearing phases ranging from 5 to 20 vol% provide benefits to the high-temperature strength and oxidation performances [2-8]. In particular, experimental values exceeding 600 MPa were reported upon flexural strength tests above 1500°C [3,8]. In addition, decreased oxidized thickness was claimed for the addition of WC to both ZrB_2- and HfB_2- based composites [2,4]. Some hypotheses have been suggested to explain the role of W-carrying compounds in the metal diboride matrices, but no conclusive mechanism has been proposed yet.

As far as the effect of WO_3 on the growing oxide scale during exposure to air at high temperature, it forms a eutectic with ZrO_2 at 1273°C [9]. This liquid phase helps the porous outermost scale to sinter and thus limit oxygen inward [2]. Another documented phenomenon involves the borate-glass formed. Kezmedashi et al. showed that 4 mol% W added to B_2O_3 increases the glass stability at higher temperature, thus hindering its volatilization, so that also this factor could be beneficial to the retention of a compact

* Corresponding author: L. Silvestroni
Tel. +39 546 699723
Fax. +39 546 46381
e-mail. laura.silvestroni@istec.cnr.it

outermost oxide scale [10]. The same conclusion was drawn upon experiments on HfB_2 carried out at Wright Patterson Labs, where a more viscous phase separated glass was found in the outermost regions of the external scale and a denser inner HfO_2, slowing down the inward oxygen penetration to the sample core [4].

Other hypothesis on the excellent high temperature flexure strength of the ZrB_2-SiC-WC system, which is also related to the oxidation behavior, was suggested by Zou et al. [3], who supposed that strength retention, or even its increase at high temperature, was due to oxide removal from grain boundaries and to a switch in the fracture mode from trans-granular to inter-granular. In a recent study, the excellent mechanical response of this system in an oxidizing environment at 1500°C was explained in terms of a combination of favorable conditions including the formation of a continuous glassy layer upon oxidation that effectively healed surface flaws, together with the extensive formation of core-rim sub-structures with shell-to-shell grain boundaries depleted of secondary phases [8]. The shell sub-structures, constituted by $(Zr,W)B_2$ solid solutions with accumulation of dislocations at the core-rim interfaces were considered beneficial for plastic deformation to accommodate the stresses under loading at high temperature [8].

Although all these explanations are plausible, no basic study has been undertaken to investigate the microstructure evolution at nanoscale level upon exposure to oxidizing environment. Such investigations would be indeed fundamental to disclose the effective role of W in the improved behavior of W-doped transition metal diborides in view of tailoring them as highly performing structural ceramics.

The oxidation behavior of a ZrB_2-WSi_2 composite upon oxidation from 1200 to 1800°C was previously investigated [11]: it was observed that this system develops a complex multi-layered scale containing zirconia, a partially protective silica-based glass and W-oxides. In the sub-surface layer, no Si-depletion layer was ever observed at any temperature, but columnar ZrO_2 started forming from 1500°C, owing to convection phenomena which made zirconia grow in the form of pillars, similar to what was observed for ZrB_2-SiC composites [12-13]. The oxidation experiments at 1800°C showed that no dense and compact external layer or stable oxidation products in the sub-surface formed; on the contrary, continuous migration of silica species and W-oxides to the top surface induced the formation of craters and fissures, owing to extensive gas escape, strongly limiting high-temperature performance.

In this paper, we put forward the picture of the microstructure evolution of a hot-pressed ZrB_2 ceramic, initially batched with 15 vol% of WSi_2, upon oxidation at 1650°C. TEM analysis was here the main tool employed to disclose the chemistry, crystallinity and composition of the new phases formed.

2. Experimental procedure

15 vol% of WSi_2 was used as sintering additive to densify ZrB_2, starting from the following commercial powders: hexagonal ZrB_2 (H.C. Starck, Germany, Grade B), specific surface area 1.0 m^2/g,

impurity max content (wt%): C: 0.25, O: 2, N: 0.25, Fe: 0.1, Hf: 0.2, particle size range 0.1-8 μm; tetragonal WSi_2 (Sigma Aldrich, Italy), -325 mesh, 99.5%, traces of metals <6000 ppm.

The powders were weighed in proper amount and mechanically mixed for 24 hours in absolute ethanol using ZrO_2 milling media. Subsequently the slurry was dried in a rotary evaporator and sieved through 250 μm screen. 30 mm-diameter pellet was green shaped by uniaxial pressing at 20 MPa. The pellet was then directly placed in the furnace and hot pressed in low vacuum (~100 Pa) using an induction-heated graphite die with an uniaxial pressure of 30 MPa increased to 40 MPa at 1930°C and dwelled for 40 minutes.

The resistance to oxidation was studied using a bottom-loading furnace (Nannetti FC18, Faenza, Italy) exposing a rectangular coupon 13.0 x 2.5 x 2 mm^3 for 15 minutes to the effect of stagnant air at 1650°C. The coupon, previously cleaned in absolute acetone and weighed, was bottom-up loaded into the hot zone of the furnace when the target temperature was achieved, elapsed 15 minutes and rapidly cooled down to allow air-quenching.

The microstructures before and after oxidation were analyzed on fractured and polished cross-sections by field-emission scanning electron microscopy (FESEM, mod. ΣIGMA, ZEISS NTS Gmbh, Germany) coupled to an energy dispersive X-ray micro-analyzer (EDS, mod. INCA Energy 300, Oxford instruments, UK).

Samples for TEM analyses were prepared by cutting 3 mm discs from the as-sintered pellet and from the coupon oxidized at 1650°C. These were mechanically ground down to about 20 μm and then further ion beam thinned until small perforations were observed by optical microscopy. Local phase analysis was performed using transmission electron microscopy (JEOL JEM 2100F) operating at a nominal voltage of 200 keV and equipped with an energy-dispersive X-ray system (EDS, mod. INCA Energy 300, Oxford instruments, UK). Electron diffraction patterns identification was carried out through the software tool developed for DigitalMicrograph [14].

Key microstructural features like residual porosity, mean grain size and volumetric content of the secondary phases were evaluated from FESEM micrographs elaborated with the support of the commercial software package Image Pro Plus (v.7, Media Cybernetics, USA).

The reaction paths leading to the final products observed in the oxidized specimen were tracked by means of the commercial package HSC Chemistry v. 6.1 (Outokumpu research Oy, Pori, Finland).

3. Results and Discussion

3.1. As sintered microstructure

The crystalline phases detected by XRD in the as-sintered ceramic (not shown) were hexagonal ZrB_2, tetragonal WB and minor amount of WSi_2. Actually, the splitting of ZrB_2 peaks for 2-theta angles above 90° was interpreted as due to the formation of a hexagonal $(Zr,W)B_2$ solid solution with shorter cell parameters if compared to the stoichiometric ZrB_2 [5].

The microstructure of the as-sintered composite is depicted in Fig. 1. In analogy with other diborides sintered with transition metal disilicides or carbides [3,5-7,15], the matrix, with mean grain size in the order of 3.5 μm, displayed a sub-structure defined as "core-shell": pure ZrB_2 constituted the core and an epitaxial $(Zr,W)B_2$ solid solution the shell, with a Zr-to-W atomic ratio of 98-to-2, Fig. 1a. The estimated volume amount of solid solution, close to 50% of the diboride matrix, confirmed an extensive development of the W-doped shell sub-structures. Dislocation pile-ups were present at the core/shell interface, owing to elastic modulus and thermal expansion mismatch arising during cooling between pure ZrB_2 and the W-containing solid solution, Fig. 1b.

Agglomerates of W-containing phases, estimated via image analysis in a cumulative amount around 5 vol% thanks to a bright Z-contrast in Fig. 1a, were identified by TEM as WB, WSi_2 and W-C-O in triangular shape or trapped at the grain junctions, Fig. 1d,e. All these secondary phases contained traces of Zr. In addition, WB, a reaction product formed upon interaction between WSi_2 and B_2O_3 covering the boride particles, showed 2-5 nm wide nano-domains, Fig. 1f, indicating possible ordered vacancies. About 3 vol% of SiO_2 pockets trapping ZrO_2 particles were also observed Fig. 1c. High resolution TEM analysis revealed clean interfaces both in case of simple triple junctions, Fig. 2a, and in case of segregation of secondary phases at the triple points, Fig. 2b. Several interfaces were analyzed in high resolution mode and no amorphous film was found between $(Zr,W)B_2$, W-C-O, WSi_2 and WB grains, as the examples in Fig. 2c,d.

3.2. Microstructure upon oxidation at 1650°C

X-ray diffraction of the surface of the oxidized specimen at 1650°C (not shown) revealed that the main crystalline phase is monoclinic ZrO_2, with only little traces of the tetragonal polytype. No clear evidence of tungsten oxide or boride was detected.

On the surface, the oxidation gave rise to an the external morphology which appears wavy and irregular, showing craters and cabbage-like structures, Fig. 3a,b. The ZrO_2 grains are as coarse as about 2 μm within a silica continuous layer. Surface uplifts, associated to the tetragonal-to-monoclinic phase transformation of ZrO_2, and growing planes are well visible in Fig. 3c. At the ZrO_2 grain boundary, no W-rich phase was found, conversely to what was observed upon oxidation at lower temperatures [11].

FESEM images of the oxidized fractured cross section in Fig. 4 show a multilayered architecture. Moving inward from the outermost scale, a discontinuous surface silica scale, a few microns thick, covers rounded ZrO_2 grains: this mixed SiO_2/ZrO_2 scale is around 40 μm thick, Fig. 4b. No continuous SiO_2 layer formed due to the lack of residual Si-carrying phases after sintering and to the coarsening of ZrO_2 grains which render the surface very uneven.

Going further deeper inside, around 180 μm of columnar ZrO_2 partially filled with silica followed and the columnar grains were better sculpted in the higher region of the scale, Fig. 4c. At the boundary between the outermost ZrO_2 and the beginning of the columnar region, Fig. 4c, W-based agglomerates, as

large as 3 μm, were found among ZrO_2 grains and their abundance decreased going towards the un-oxidized bulk. In addition, W-based tiny droplets are homogeneously dispersed over the entire Zr-oxide thickness, from the boride interface up to the end of the columnar ZrO_2, Fig. 4d. The oxide layer is well anchored to the un-oxidized bulk with a sharp interface, Fig. 4e, suggesting that the oxidation front proceeded transgranularly instead of intergranularly, similar to what was reported for other ZrB_2-composites containing W-based compounds [8].

TEM analyses carried out on the oxidized sample enabled to disclose finer microstructural details. First of all, the outermost silica-based glass was found to be completely amorphous, without traces of crystalline nano-precipitates, as testified by the diffraction patterns in Fig. 5. The contrasts visible in Fig. 5b are due to chemical variations of the SiO_2-based glass and include little amount of dissolved Zr, W and other impurity cations, like Ca and Al.

The outermost ZrO_2 was typified by a defective structure: dislocations, twinning and stacking faults were regularly observed, as a result of the tetragonal to monoclinic transformation, Fig. 6. No W trace was detected by EDX analysis inside the ZrO_2 grains, confirming the negligible solubility of W in the Zr-oxide lattice.

Moving inward, the glassy phase which runs along the columnar ZrO_2 grains has a varying composition containing traces of Zr, W and Al, but in this case, crystalline precipitates can be easily found, (see the rounded area in Fig. 7).

At the interface between the outermost rounded ZrO_2 grains and the columnar ones, in the area illustrated in the FESEM image of Fig. 4c, faceted particles with dark contrast and hexagonal shape were found embedded in a SiO_2 based glassy phase, Fig. 8a. EDX analysis coupled to electron diffraction revealed these dark particles to be cubic W, with Zr in a ratio around 85:15 at%, Fig. 8b. The glassy phase well wets the metallic particles, Fig. 8b-d. Also at this depth, no W-traces were found in monoclinic ZrO_2 grains, as confirmed by the EDX spectra in Fig. 8c. In the same area, in proximity of these W,Zr metallic particles, monoclinic WO_3 whiskers were often found, Fig. 9. This phase had a stringy aspect when not oriented, Fig. 9a and assumed a whiskers or rod-like shape once oriented, Fig. 9b,d. The electron diffraction image of the whisker in Fig. 9c shows that the growth direction of the monoclinic WO_3 occurred along the [001] direction and a striking feature is found in the diffraction spots. This is due to stacking faults possibly related to oxygen deficiencies, that are commonly observed in tungsten oxides [16]. The WO_3 rods were surrounded by SiO_2-based glass, containing traces of W and Zr, Fig. 9e.

These phases could be the oxidation products of the secondary phases present in the as-sintered microstructure. This assumption is based on two facts. First, these pockets have similar size as the pristine W-based phases (some micrometers) and secondly, the metallic particles contains comparable amount of Zr, as detected in the residual WB, WSi_2 and W-C-O.

Entering deeper into the oxidized sub-scale characterized by columnar features, monoclinic ZrO_2 grains were externally and internally adorned with bright nano-droplets of variable size from 5 to 60 nm, Fig. 10. The inner ones acted as pins for the advancement of the dislocations front inside ZrO_2, Fig. 10c. High resolution TEM images coupled to chemical and structural analyses revealed these droplets to be cubic W with some oxygen trace, nestled in large ZrO_2 grains, Fig. 11. Their spherical shape suggests a very low wettability of W towards Zr-oxide. In addition, these tiny particles were always found adjacent to some glassy pockets, as shown in the high resolution TEM image of Fig. 11c. The morphology of these zirconia grains with W encapsulated inclusions presented in Fig. 10 let us presume that these are an oxidation solid product of the original $(Zr,W)B_2$ solid solution, as it will be discussed later. Such W-nano-droplets resisted against the oxidation attack thanks to their formation depth, which locally guaranteed oxygen partial pressure below the predominance stability threshold ($\log_{10}P_{O2}$<7 at 1650°C). It assumed that, at 1650°C, the W released in proximity of the external surface tended to form WO_3 and immediately volatilized [17], thus leaving inclusions-free ZrO_2 grains that progressively filled the voids upon coalescence and coarsening mechanisms at high temperature.

3.3. Thermodynamics

In order to understand the oxidation mechanism of this W-doped ZrB_2 composite, thermodynamic calculations were performed through the HSC commercial software package. Unfortunately, WB_2 compound was not present in the HSC database, so we could not directly compare its tendency to oxidize, and indirectly that of the $(Zr,W)B_2$ solid solution, with that of pure ZrB_2. Due to this lack of thermodynamic data, in this paragraph we can track the oxidation of the pure ZrB_2 compared to the other W-based compounds, WB, WSi_2 and WC and only make some cautious comments on the solid solution oxidation behavior.

Fig. 12 presents the thermochemical equilibrium of a simplified composite computed at 1650°C and 1 bar of isobaric pressure with increasing oxygen amount and starting composition equal to 0.7 kmoles of ZrB_2 and equivalent amount of WB, WSi_2 and WC, 0.1 kmoles each.

The plot provides some important indications that will be discussed in the following.

- Starting from the left side of Fig. 12, ZrB_2, WSi_2 and WC progressively oxidize even in presence of only traces of oxygen, according to reactions R1, R2 and R3, respectively:

  $ZrB_2 + 2.5O_2\,(g) \rightarrow ZrO_2 + B_2O_3(l)$ R1

  $WSi_2 + 2O_2\,(g) \rightarrow W(s) + 2SiO_2\,(l)$ R2

  $WC + 0.5O_2\,(g) \rightarrow W(s) + CO(g)$ R3

- According to R1, the oxidation of ZrB_2 should provide the same molar amount of oxide products, but the plot in Fig. 12 shows that the amount of B_2O_3 developed is lower than that of ZrO_2, suggesting some recombination reactions, presumably with the available free W coming from R2 and R3. A

plausible explanation is the formation of the WB phase, which increases in amount accordingly. The overall reaction can therefore be condensed to R4:

$ZrB_2 + WSi_2 + WC + 2.5O_2 \rightarrow ZrO_2\,(s) + 2WB(s) + 2SiO_2\,(l) + CO(g)$ R4

- WB compound is stable as condensed phase even with relatively high amount of oxygen (1.7 kmoles), when ZrB_2, WSi_2 and WC are already totally consumed. This finding is quite relevant as it confirms the better oxidation behavior of WB over the other species. If this improved behavior applies also to the $(Zr,W)B_2$ solid solution, we could explain the trans-granular oxidation front observed in the cross section.
- W (and B_2O_3) formation abruptly increases in correspondence of the starting of consumption WB, indicating this phase is a source of elemental W. Similarly, and given the large and spread amount of W found in the microstructure, we can infer that the $(Zr,W)B_2$ solid solution is the major W origin.
- Metallic W is formed and stable with low molar amount of oxygen, i.e. at low PO_2, whilst WO_3 is favored as condensed phase at high PO_2. In addition, W and WO_3 have a coexisting field. This explains why the W nano-droplets and particles are preserved all throughout the subsurface and why WO_3 is found mostly in the upper zone of the columnar ZrO_2 scale.
- The plot foresees the formation of WO_2 under certain conditions, but this phase was not found in the oxidized microstructure. The W-O phase diagram has been largely discussed, but not fully accepted [18], however it has been reported that WO_2 vaporizes by disproportionation to gaseous tungsten trioxide and solid W. In addition, Blackburn et al. observed that WO_2 heated at 1051 to 1385°C gave WO_3 as condensate vapor plus unevaporated residue of W [19], similar to our experimental observations (Fig. 8a).
- Aware that residual WSi_2 is only a minor phase in the as-sintered composite, we can however see that at high PO_2 the formation of SiO_2 is favored over the evolution of gaseous SiO, therefore the silica formed on the surface, even if discontinuous, will be stable and provide localized protection against oxygen inward diffusion. Conditions for the development of volatile SiO will be met only in the subsurface layer at low oxygen partial pressure, estimated to be in the order of 10^{-10}-10^{-14} Pa [20].

To sum up the major outcomes emerged from these thermodynamic computation, we can say that WB has a better oxidation resistance than any other compound present in this system and, at low oxygen partial pressure, its formation is even favourable upon oxidation of the other phases.

3.4 Oxidation behavior

Upon combination of the microstructural features observed in the quenched specimen and the thermodynamic computations, an oxidation mechanisms occurring at 1650°C for this W-doped ZrB_2 composite is discussed in the following and Fig. 13 sketches the morphology evolution.

The as-sintered matrix is constituted by ZrB_2 grains homogeneously surrounded by about 50 vol% of $(Zr,W)B_2$ solid solution, then around 5 vol% of crystalline W-carrying phases (in abundance order as WB, WSi_2, and WC) are segregated at the triple junctions and about 3 vol% of silica is also present, as dissociation product of WSi_2 during sintering [5], Fig. 13a.

The oxidation of the ZrB_2 matrix yields B_2O_3 and ZrO_2 (R1). The solid solution around the ZrB_2 grains oxidizes as well: given the negligible solubility of W in ZrO_2, as reported from the Zr-W-O phase diagram [18] and confirmed by the EDX analyses in Fig. 6c and 8c, W is released as metal within the growing ZrO_2. Therefore the overall oxidation reaction involving the solid solution can be expressed as:

$$(Zr_{1-x}W_x)B_2 + 2.5(1-x)\ O_2 \rightarrow (1-x)\ ZrO_2 + x\ W(s) + B_2O_3(l,g) \qquad R5$$

Of these products, only ZrO_2 can be found in the outermost scale, Fig. 5b, since W promptly oxidizes into highly volatile W oxides, according to R6 [21]:

$$W + O_2 \rightarrow WO_2 + 0.5O_2 \rightarrow WO_3 \rightarrow W\text{-}O(g) \qquad R6$$

The voids left by the progressive oxidation and volatilization of the metal inclusions from the surface are filled by the growing ZrO_2, explaining a multi-step process of cell distortion and defects creation, Fig. 13b. On the contrary, in the subsurface scale, W is retained encased in ZrO_2 grains together with little amount of glass, Fig. 11c. It is worthy to underline that the W-droplets were found all across the ZrO_2 grains and not just in localized domains, i.e. the oxide does not preserve the core-shell morphology. This could indicate that when W is expelled by the oxidizing solid solution it is quite mobile, presumably in vapor phase, and is able to spread across the growing ZrO_2 also in the area occupied by the original pure ZrB_2. Only upon cooling it can condensate as metallic droplets throughout all the ZrO_2 volume. Indeed, extensive studies on the volatilization of tungsten conducted by Gulbrasen in the 50-60s concluded that above 1000°C pressure has a minor impact on the tungsten oxidation rate compared to the temperature effect [22] and even more recent investigations on the oxidation behavior of pure tungsten in the 400-900°C temperature interval carried out with a maximum partial pressure of $\sim 5 \cdot 10^{-6}$ atm confirmed that volatilization of tungsten-oxide assumes significance already above 750°C [23]. Therefore, the hypothesis of volatile W-phases across the oxide layer during the test at 1650°C is very likely.

Simultaneously, residual WSi_2 and WC start oxidizing into W, liquid SiO_2 and gaseous CO (R2-R3): the availability of fluid silica provides localized protection against the oxygen diffusion. Further contribution to the formation of the outermost silica scale derives from the SiO_2 already present in the material upon sintering. B_2O_3, coming from the oxidation of the diboride matrix (R1), dissolves into silica decreasing its viscosity and melting point from 1730°C to 1470°C (for less than 10 mol% of B_2O_3 dissolved into silica) [24]. As soon as an outermost local silica lid is formed, it acts as localized protection for the products underneath, therefore W-oxide and metal residues can be retained as solid phases, Fig. 13c. The local formation of W(Zr) particles in this region in hexagonal shape could be due to variations in the vapor conditions, which strongly influence the shape and morphology of the condensed products [25].

With the advancing of the oxidation front, the oxide scale further thickens, thus decreasing the oxygen partial pressure at the bottom of the subsurface scale. Under these conditions, W is safe inside the ZrO_2 grains, but volatile products like W-oxides and SiO, start to develop. Therefore, the formation of gases at 1650°C is then the driving force for the starting growth of columnar ZrO_2 from the inner oxidizing bulk, Fig. 13d. The W droplets found covering ZrO_2 grains could be a consequence of vapor condensation after quenching. As a result of the abundant leak of volatile species, the development of large ZrO_2 columns is favored in the subsurface, whilst on the surface ZrO_2 precipitates, given its limited solubility in the glass, and progressively coarsens.

According to the mechanism here proposed and to previous analysis on the oxidation behavior of this composite at temperatures up to 1800°C [11], one can deduce that, once the columnar scale has formed, the oxygen inward will be always faster and the oxidation will proceed with a parabolic behavior. As such, we tend not to share the idea of an improved oxidation behavior of ZrB_2 composites containing solely W-compounds at temperatures exceeding 1650°C, since W and W-O phases will quickly vaporize to volatile species. However, we agree that the picture of the oxidation behavior could assume a notably different trend when enough amount of SiC is simultaneously present in the boride matrix [4].

3.5 What is the role of W in the oxidation behavior of ZrB_2?

In the light of the present investigations, we can outline the main effects of W-compounds during the oxidation of ZrB_2.

Firstly, it has an indirect impact, because, upon sintering, it promotes the development of a microstructure with clean grain boundaries and only refractory phases at the triple junctions. As a consequence, the advancement of the oxidation front proceeds in a coherent and transgranular mode, instead of an intergranular one. This is mainly due to the absence of soft phases at the triple points, and also to a better oxidation resistance of the WB phase, as compared to pure ZrB_2. This even oxidation boundary can be beneficial for temperature regimes up to 1650°C, but we can expect that an excessive coarsening of the columnar ZrO_2 will be catastrophic for the onset of large coefficient of thermal mismatches between the boride and the oxide layer that will lead to spallation.

As a direct role of W we have to distinguish two cases: from the solid solution and from the secondary phases.

In the case of the $(Zr,W)B_2$ solid solution, we have demonstrated that it evolves into finely dispersed W nano-droplets encapsulated by large ZrO_2 grains. We can envision that when oxygen reaches these metallic droplets, they will oxidize to W-O expanding their volume and slowing down the oxidation kinetics, as the W-O phases are stable as condensed phases at high oxygen partial pressure. This phenomenon can be effective at lower temperatures [21], but at 1650°, volatilization will occur. However, the formation of oxides that, at certain depths of the ceramic, are stable as condensed phases or cations that dissolved in

the glass increase its viscosity and induce phase separation (Zr, W), could be favorable conditions to retard oxidation.

Some authors suggested that tungsten oxide species form strong acid sites in ZrO_2 and inhibit ZrO_2 tetragonal to monoclinic polytype transformations [26]. In this and previous studies [5,11], X-ray diffraction and electron diffraction revealed only the monoclinic polytype at any depth level. Therefore we tend to attribute a minor role to W in the stabilization of tetragonal ZrO_2.

As for the W-bearing secondary phases, WSi_2 and WC oxidize to W or WO_3 depending on the oxygen partial pressure and additional WB phase, which we have shown to be the most oxidation resistant, will form by recombination of W and boron oxide. However, at such high temperature, tungsten oxides will volatilize quickly, [21] promoting convective phenomena and effervescence.

Hence, in a nutshell, high resolution TEM analyses revealed new fundamental findings that enabled to understand the high-temperature behavior of W-doped ZrB_2 compounds and yelding insight into the oxidation behavior of the boride solid solution.

4 Conclusions

A W-doped ZrB_2 composite was analyzed by transmission electron microscopy in the as sintered state and upon oxidation at 1650°C in static air. The matrix was composed of a $(Zr,W)B_2$ solid solution in a core/shell structure with WB, WSi_2 and WC refractory phases at the triple point junctions, all characterized by grain boundaries free of amorphous phases.

This composite after high temperature oxidation evolved into a multilayered architecture with a thin outermost thin SiO_2-based glass, a coarse rounded ZrO_2 scale partially filled with glass, a columnar ZrO_2 well anchored to the unreacted bulk. TEM analysis confirmed a negligible solubility of W into the ZrO_2 lattice, but rather the ejection of W nano-droplets encased into ZrO_2 grains along all the oxidized sample thickness. W particles and WO_3 whiskers embedded into silica-based pockets were also detected across the oxide scale at different depths depending on the local oxygen partial pressure.

The detailed microstructural analysis combined with the thermodynamics allowed to propose an oxidation mechanism and to define the stability fields of the various W-compounds.

Acknowledgements

Part of the research leading to these results has received funding from the European Community's Seventh Framework Programme (FP7/2011-2014) under grant agreement LIGHT-TPS No. 607182.

References

1. E. Wuchina, E. Opila, M. Opeka, W.G. Fahrenholtz, I. Talmy, UHTCs: Ultra-High Temperature Ceramic Materials for Extreme Environment Applications, The Electrochem. Soc. Interf. (Winter 2007) 30-36.

2. S.C. Zhang, G.E. Hilmas, W.G. Fahrenholtz, Improved oxidation resistance of zirconium diboride by tungsten carbide additions, J. Am. Ceram. Soc. 91 (2008) 3530-3535.

3. J. Zou, G.J. Zhang, C.F. Hu, T.Nishimura, Y. Sakka, J. Vleugels, O. Van der Biest, Strong ZrB_2-SiC ceramics at 1600°C, J Am Ceram Soc. 95 (2010) 874–878.

4. C.M. Carney, T. A. Parthasarathy, M.K. Cinibulk, Oxidation resistance of hafnium diboride ceramics with additions of silicon carbide and tungsten boride or tungsten carbide, J. Amer. Ceram. Soc. 94 (2011) 2600-2607.

5. L. Silvestroni, D. Sciti, TEM analysis, mechanical characterization and oxidation resistance of a highly refractory ZrB_2 composite, J. Alloys & Comp. 602 (2014) 346-355.

6. D.L Hua, Q. Zheng, H. Gu, D-W Ni, G-J Zhang, Role of WC additive on reaction, solid-solution and densification inHfB_2–SiC ceramics, J. Europ. Ceram. Soc. 34 (2014) 611–619.

7. H.B. Ma, Z.Y. Man, J.X. Liu, F.F. Xu, G.J. Zhang, Microstructure, solid solution formation and high-temperature mechanical properties of ZrB_2 ceramics doped with 5vol% WC, Mater. & Design, 81 (2015) 133-140.

8. F. Monteverde, L. Silvestroni, Combined effects of WC and SiC on densification and thermo-mechanical stability of ZrB_2 ceramics, submitted to Corrosion Science.

9. L.L. Y. Chan, M.G. Scroger, B. Phillips, Condensed Phase Relations in the Systems ZrO_2-WO_2-WO_3 and HfO_2-WO_2-WO_3, J. Amer. Ceram. Soc. 50 (1967) 211-215.

10. M. Kazemzadeh Dehdashti, W.G. Fahrenholtz, G.E. Hilmas, Effects of temperature and the incorporation of W on the oxidation of ZrB_2 ceramics, Corros. Sci. 80 (2014) 221-228.

11. L. Silvestroni, G. Meriggi, D. Sciti, Oxidation behavior of ZrB_2 composites doped with various transition metal silicides, Corros. Sci. 83 (2014) 281-291.

12. P. Hu, W. Guolin, Z. Wang, Oxidation mechanism and resistance of ZrB_2-SiC composites. Corros. Sci. 51 (2009) 2724-2732.

13. A. Rezaie, W.G. Fahrenholtz, G.E. Hilmas, Evolution of Structure During the Oxidation of Zirconium Diboride – Silicon Carbide in Air up to 1500°C, J. Eur. Ceram. Soc. 27 (2007) 2495-2501.

14. D.R.G. Mitchell, DiffTools: Software Tools for Electron Diffraction in Digital Micrograph, Micr. Res. and Technique, 71 (2008) 588-593.

15. L. Silvestroni, D. Sciti, Densification of ZrB_2-$TaSi_2$ and HfB_2-$TaSi_2$ Ultra-High-Temperature Ceramic Composites, J. Am. Ceram. Soc. 94 (2011) 1920-1930.

16. J. Zhou, Y. Ding, S.Z. Deng, L. Gong, N.S. Xu, Z. L. Wang, Three-dimensional Tungsten Oxide Nanowire Networks, Adv. Mater. 17 (2005) 2107-2110.

17. E.A. Gulbransen, K.F. Andrew, F.A. Brassart, Kinetics of Oxidation of Pure Tungsten, 1150°–1615°C, J. Electrochem. Soc. 111 (1964) 103-109.

18. H.A. Wrledt, The O-W (Oxygen-Tungsten) System, Bull. Alloy Phase Diagr. 10 (1989) 368-384.

19. P.E. Blackburn, M. Hoch, H.L. Johnston, The Vaporization of Molybdenum and Tungsten Oxides, J. Phys. Chem., 62 (1985) 769-773.

20. W.G. Fahrenholtz, Thermodynamic Analysis of ZrB_2–SiC Oxidation: Formation of a SiC-Depleted Region, J. Am. Ceram. Soc. 90 (2007) 143-148.

21. S.C. Cifuentes, M.A. Monge, P. Pérez, On the oxidation mechanism of pure tungsten in the temperature range 600–800°C, Corros. Sci. 57 (2012) 114–121.

22. E.A. Gulbransen, K.F. Andrew, Kinetics of Oxidation of Pure Tungsten from 500°-1300°C, J. Electrochem. Soc. 107 (1960) 619–628.

23. J. Habainy, C. Nilsson, Oxidation of Pure Tungsten in the Temperature Interval 400° to 900°C, Master Thesis, Division of Materials Engineering Department of Mechanical Engineering Faculty of Engineering, Lund University, Sweden, September 2013.

24. T.J. Rockett, W.R. Foster, Phase Relations in the System Boron Oxide-Silica, J. Am. Ceram. Soc., 48 (1965) 75-80.

25. M. Weil, W.D. Schubert, The Beautiful Colours of Tungsten Oxides, Tungsten, Newsletter June 2013.

26. D.G. Barton, S.L. Soled, G.D. Meitzner, G.A. Fuentes, E. Iglesia, Structural and Catalytic Characterization of Solid Acids Based on Zirconia Modified by Tungsten Oxide, J. Catalysis, 181 (1999) 57–72.

Figures captions

Fig. 1: FESEM and TEM images showing the microstructure of the as-sintered composite. a) General overview, b) the "core-shell" structure of the matrix, c) the secondary phases, d) residual WSi_2 trapped at the grain boundaries, e) the formation of tetragonal WB with the diffraction pattern inset, and f) the structure of WB with the FTT inset showing nano-domains.

Fig. 2: TEM images of the as-sintered composite showing a) a clean triple point junction, b) newly formed WB crystallized at the triple junctions and c) - d) HR-TEM images of clean boundaries.

Fig. 3: SEM images of the external surface after oxidation at 1650°C. a) Overall appearance, b) a crater emerging from the surface, c) growing planes in ZrO_2 grains indicated by the arrow.

Fig. 4: SEM images of the cross section after oxidation at 1650°C. a) Overall appearance and magnified areas as indicated in b)-e). b) Outermost coarse ZrO_2 with silica layer on top, c) interface between the outermost ZrO_2 and the columnar ZrO_2 scale, d) W-oxide phase and W-nanodroplets spread across the ZrO_2- scale and e) sharp interface between the oxide and the boride un-oxidized bulk.

Fig. 5: TEM image of the oxidized composite showing the morphology and composition of the outermost glass among monoclinic ZrO_2 grains with corresponding diffraction pattern and EDS spectra.

Fig. 6: TEM images and diffraction patterns of the HRTEM pictures in the boxed areas evidencing defects in the outermost ZrO_2 grains: a) dislocations, b) twinning, c) stacking faults. The EDS spectrum confirms no W trace within ZrO_2 grains.

Fig. 7: HR-TEM image of the intergranular glass running through the columnar ZrO_2 grains, showing traces of crystalline compounds in the SiO_2-based glass (circled area). The insets are: a low magnification image of the zone, the EDS spectrum and the diffraction pattern of the partially crystallized glass.

Fig. 8: a) TEM image of W,Zr particles immersed in the glass within the columnar ZrO_2 grains with low-magnified view of the area inset. The HR-TEM images in b)-d) are magnified images of the boxed areas in a) and show the composition of ZrO_2, particle and glass.

Fig. 9: TEM images showing the formation of WO_3 whiskers with diffraction patterns and EDX spectra inset. c) and e) are magnification of the boxed areas in b) and d), respectively.

Fig. 10: TEM images of typical columnar ZrO_2 grains in ZrB_2-WSi_2 composite after oxidation showing encased W-droplets. Note in d) the dislocation advancement arrested by the metal spheres.

Fig. 11: HR-TEM images W nano-droplets nestled in pure ZrO_2 with EDX spectra and diffraction patterns. Note in a) and c) the presence of glass adjacent to the droplet.

Figure 12: Thermo-chemical equilibria calculated at 1650°C with 1 bar of isobaric air pressure: starting kmoles of reactants are 0.7 ZrB_2, 0.1 WB, 0.1 WSi_2 and 0.1 WC.

Fig. 13: Sketch of the oxidation phenomena occurring at 1650°C in the W-doped ZrB_2 composite.

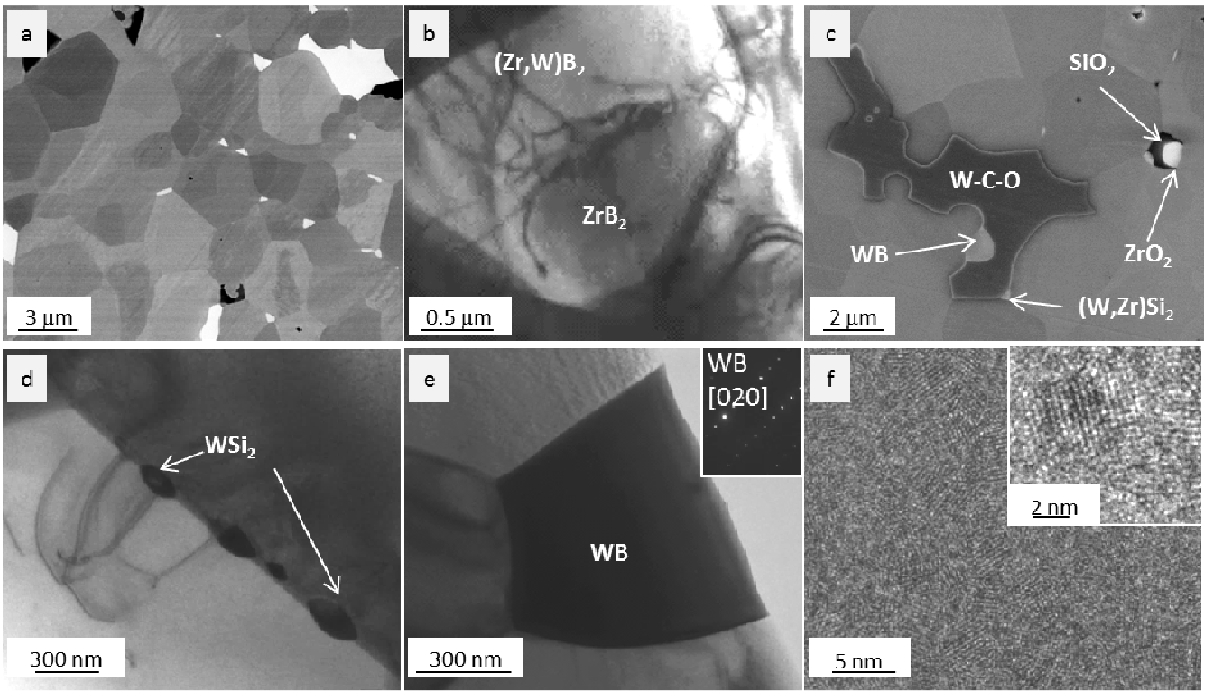

Fig. 1: FESEM and TEM images showing the microstructure of the as-sintered composite. a) General overview, b) the "core-shell" structure of the matrix, c) the secondary phases, d) residual WSi_2 trapped at the grain boundaries, e) the formation of tetragonal WB with the diffraction pattern inset, and f) the structure of WB with the FTT inset showing nano-domains.

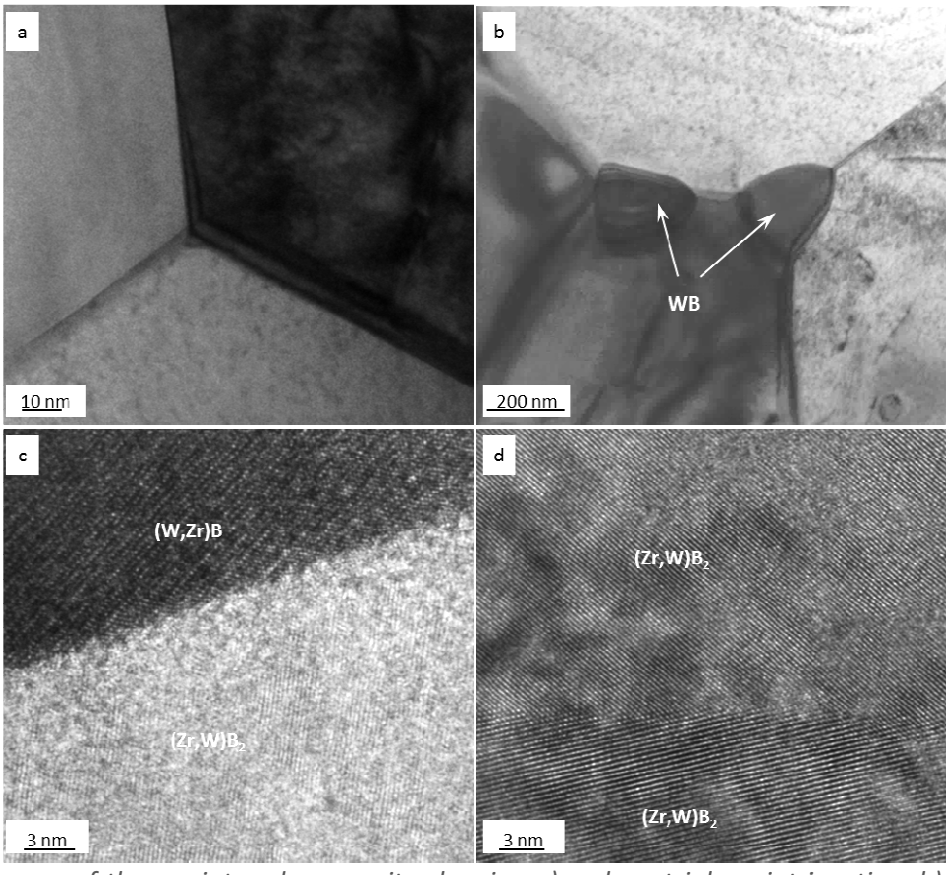

Fig. 2: TEM images of the as-sintered composite showing a) a clean triple point junction, b) newly formed WB crystallized at the triple junctions and c) - d) HR-TEM images of clean boundaries.

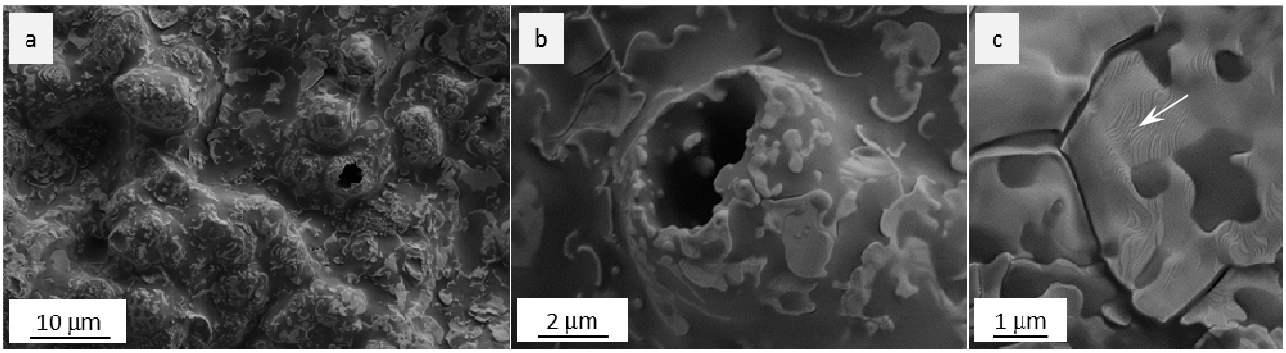

Fig. 3: SEM images of the external surface after oxidation at 1650°C. a) Overall appearance, b) a crater emerging from the surface, c) growing planes in ZrO_2 grains indicated by the arrow.

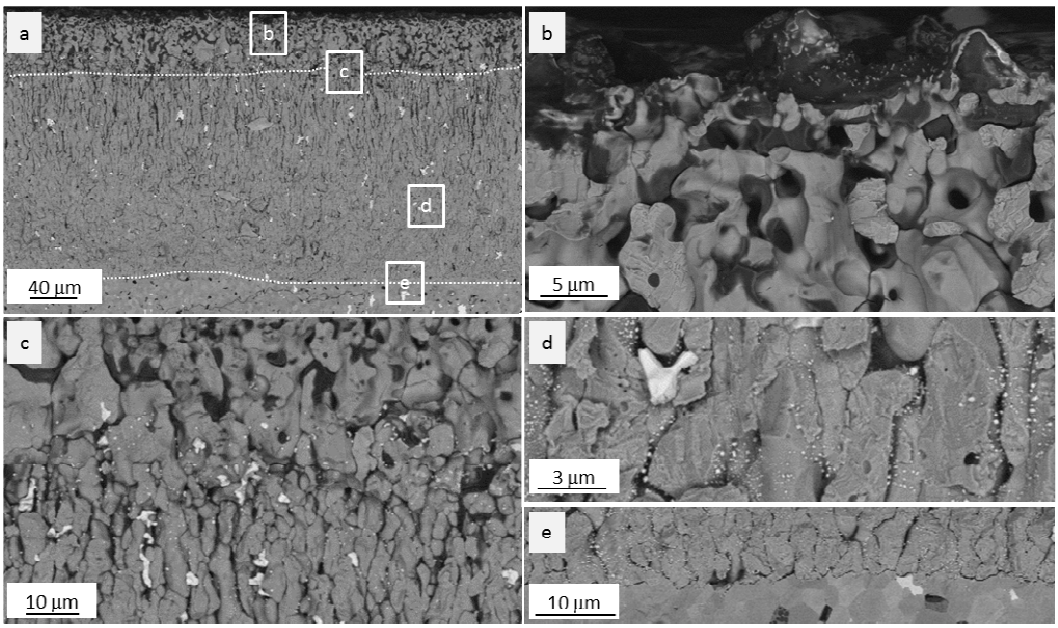

Fig. 4: SEM images of the cross section after oxidation at 1650°C. a) Overall appearance and magnified areas as indicated in b)-e). b) Outermost coarse ZrO_2 with silica layer on top, c) interface between the outermost ZrO_2 and the columnar ZrO_2 scale, d) W-oxide phase and W-nanodroplets spread across the ZrO_2- scale and e) sharp interface between the oxide and the boride un-oxidized bulk.

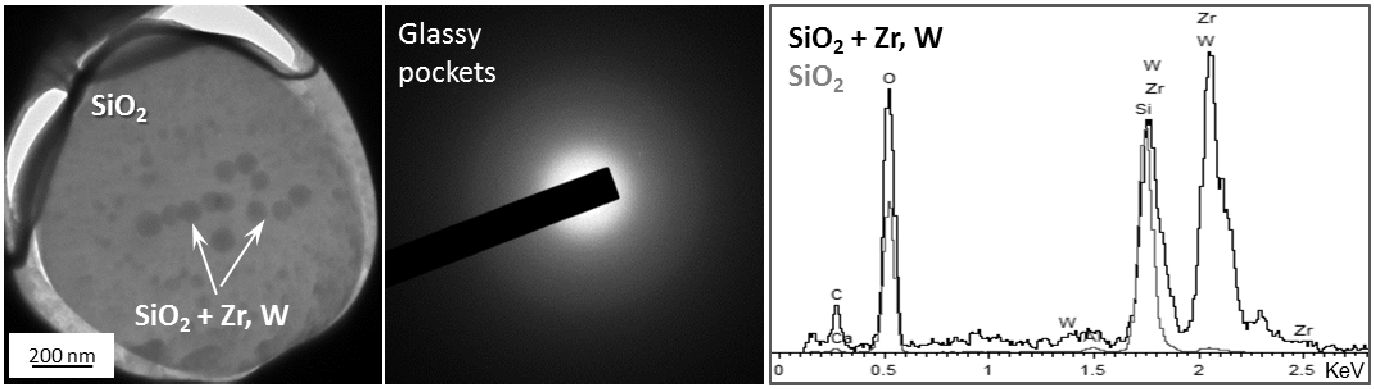

Fig. 5: TEM image of the oxidized composite showing the morphology and composition of the outermost glass among monoclinic ZrO2 grains with corresponding diffraction pattern and EDS spectra.

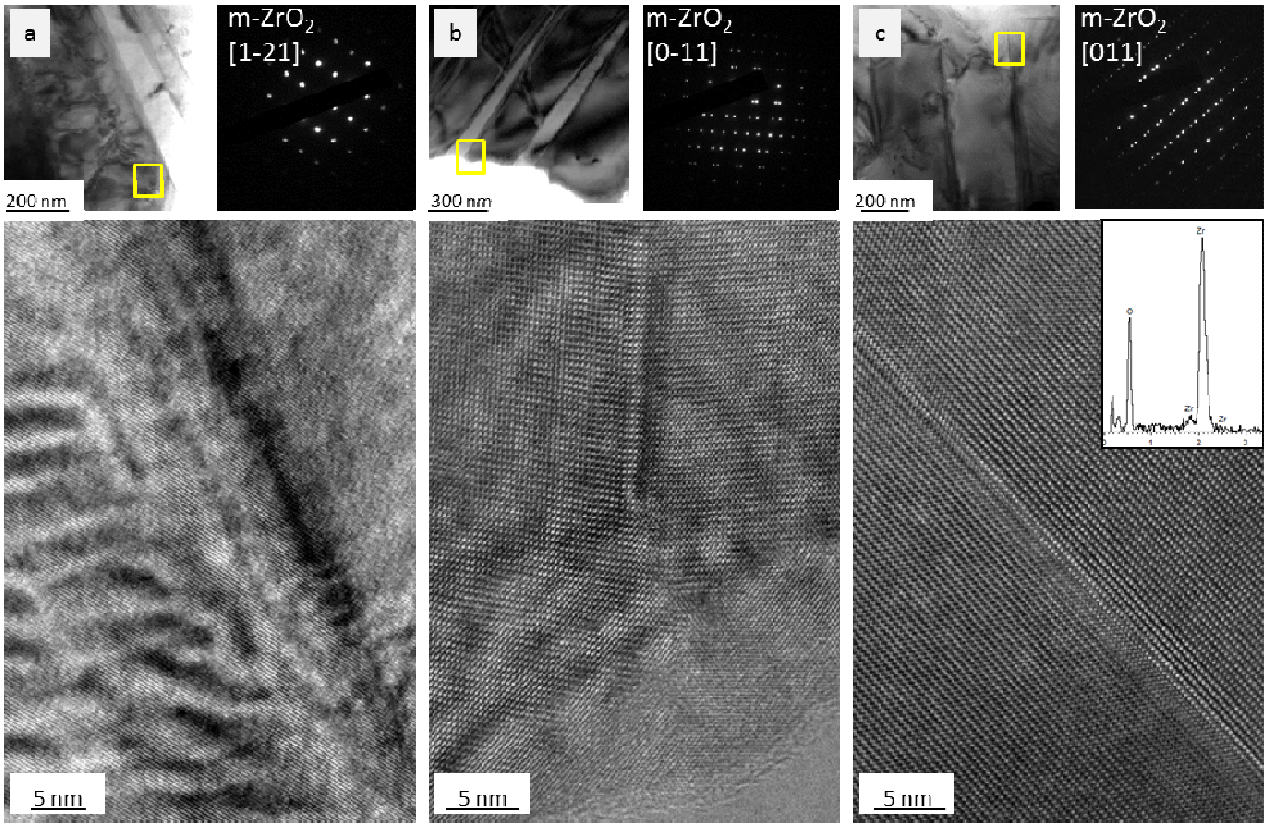

Fig. 6: TEM images and diffraction patterns of the HRTEM pictures in the boxed areas evidencing defects in the outermost ZrO_2 grains: a) dislocations, b) twinning, c) stacking faults. The EDS spectrum confirms no W trace within ZrO_2 grains.

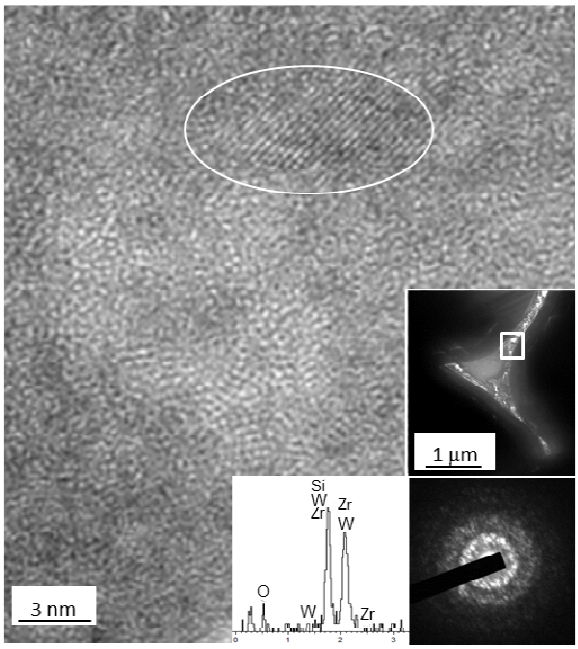

Fig. 7: HR-TEM image of the intergranular glass running through the columnar ZrO_2 grains, showing traces of crystalline compounds in the SiO_2-based glass (circled area). The insets are: a low magnification image of the zone, the EDS spectrum and the diffraction pattern of the partially crystallized glass.

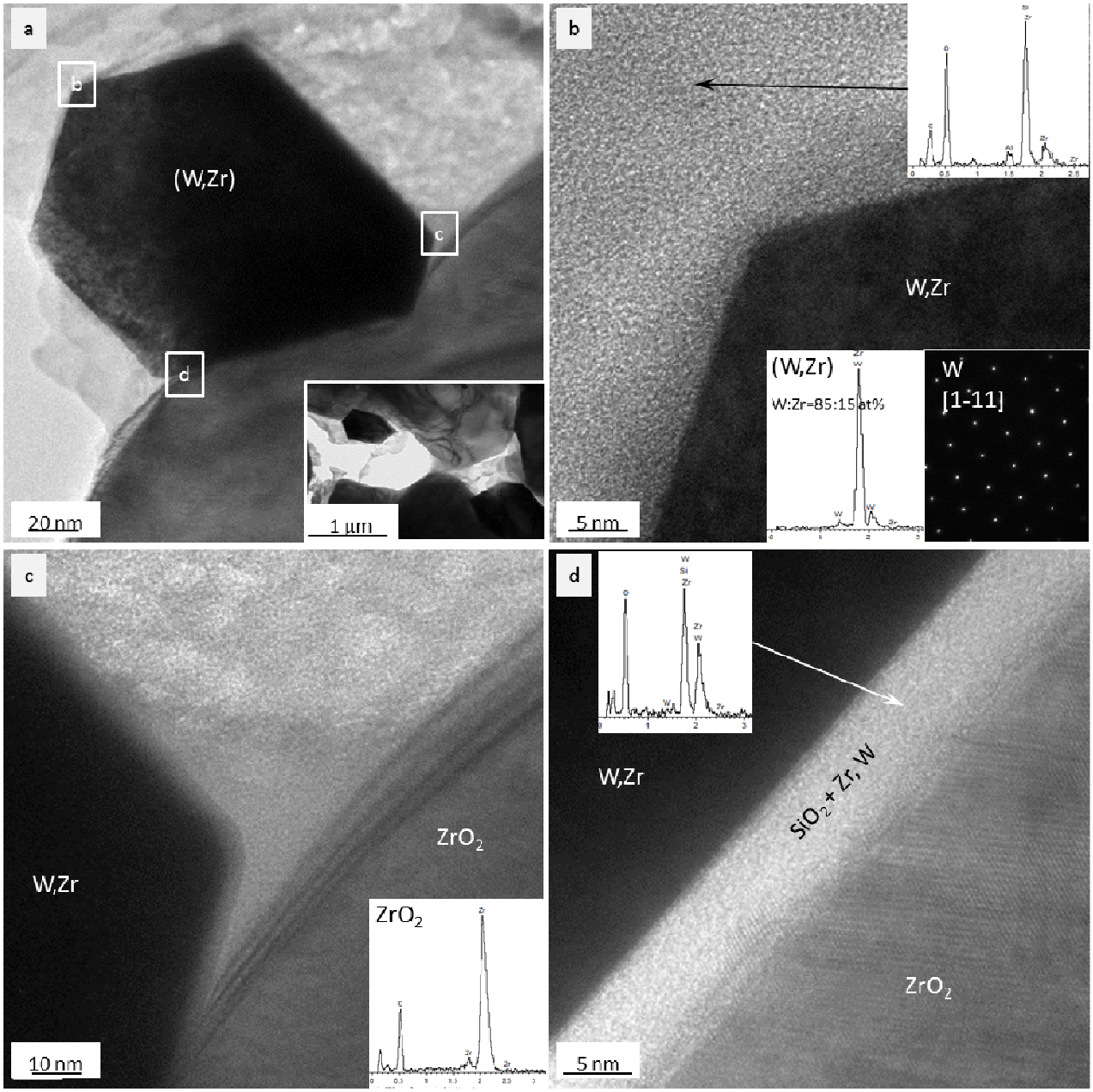

Fig. 8: a) TEM image of W particles immersed in the glass within the columnar ZrO_2 grains with low-magnified view of the area inset. The HR-TEM images in b)-d) are magnified images of the boxed areas in a) and show the composition of ZrO_2, particle and glass.

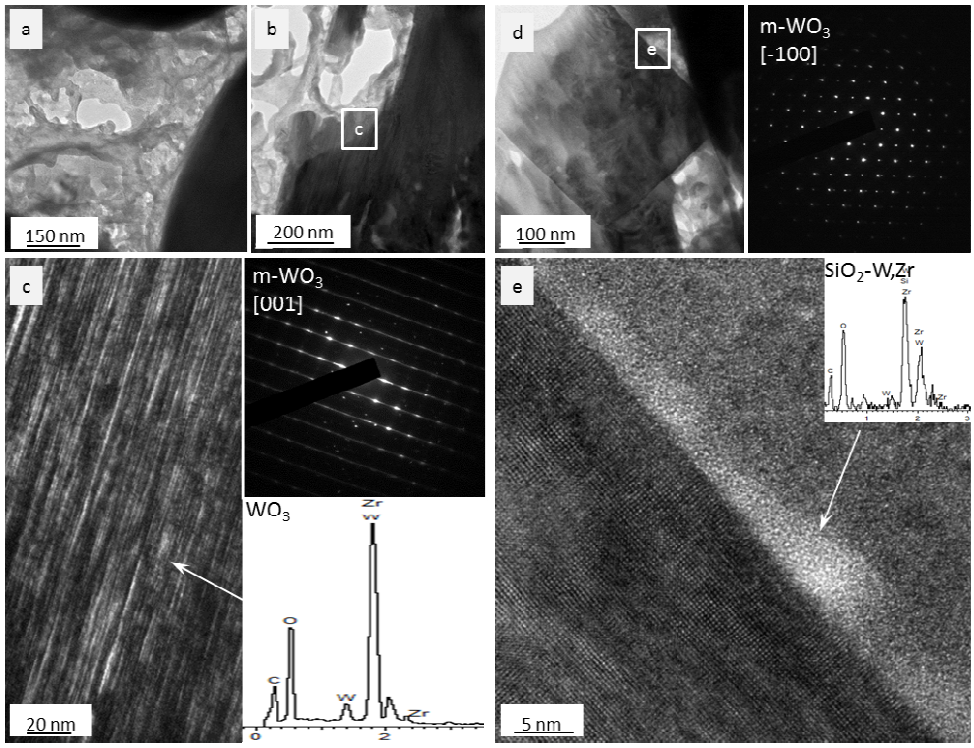

Fig. 9: TEM images showing the formation of WO_3 whiskers with diffraction patterns and EDX spectra inset. c) and e) are magnification of the boxed areas in b) and d), respectively.

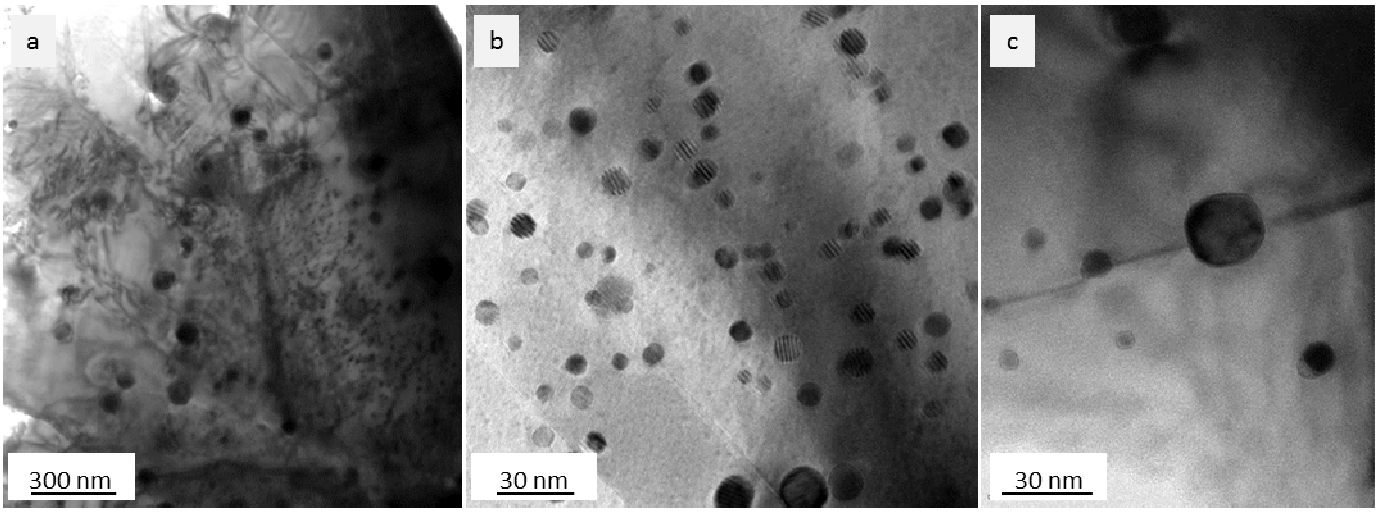

Fig. 10: TEM images of typical columnar ZrO_2 grains in ZrB_2-WSi_2 composite after oxidation showing encased W-droplets. Note in d) the dislocation advancement arrested by the metal spheres.

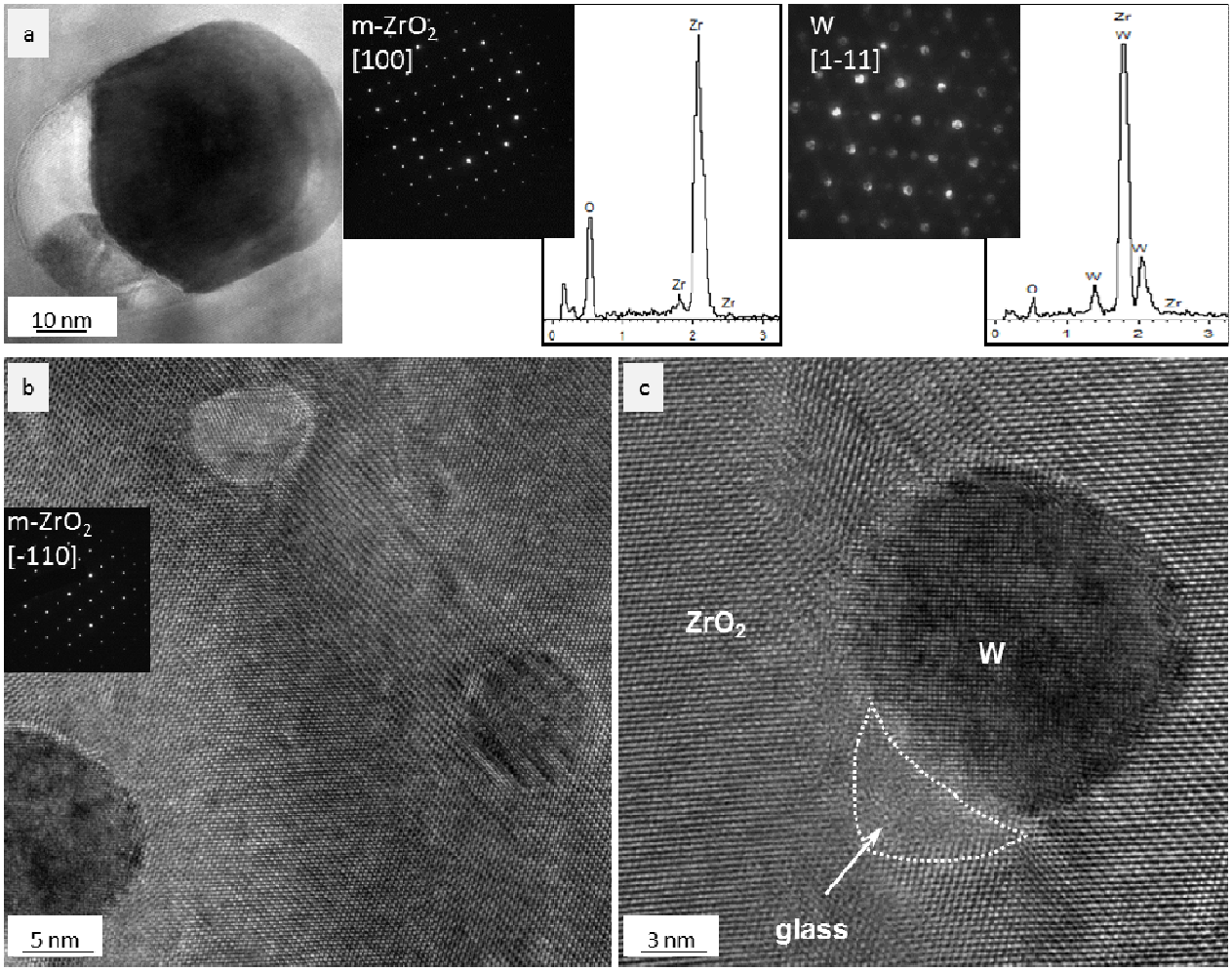

Fig. 11: HR-TEM images W nano-droplets nestled in pure ZrO_2 with EDX spectra and diffraction patterns. Note in a) and c) the presence of glass adjacent to the droplet.

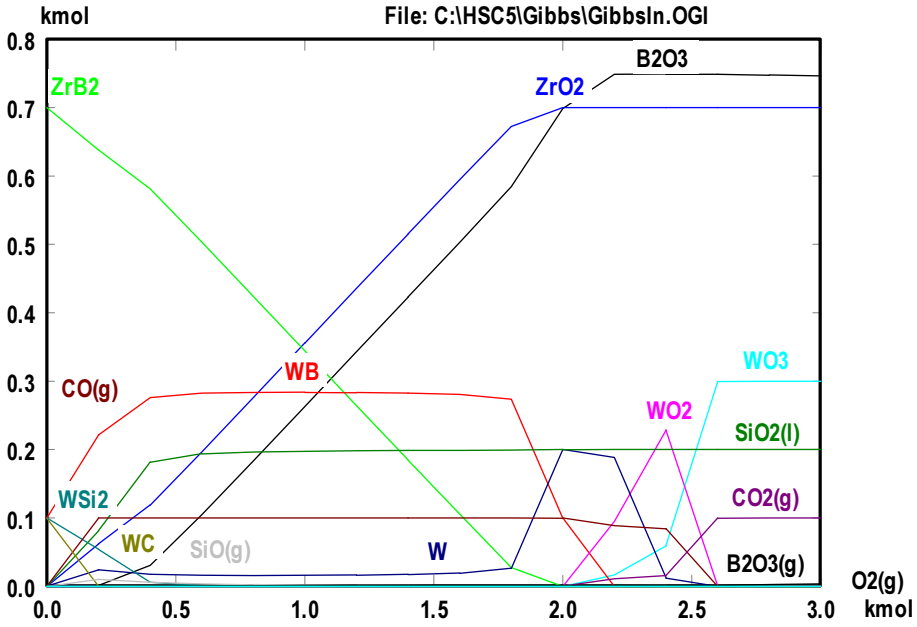

Figure 12: Thermo-chemical equilibria calculated at 1650°C with 1 bar of isobaric air pressure: starting kmoles of reactants are 0.7 ZrB_2, 0.1 WB, 0.1 WSi_2 and 0.1 WC.

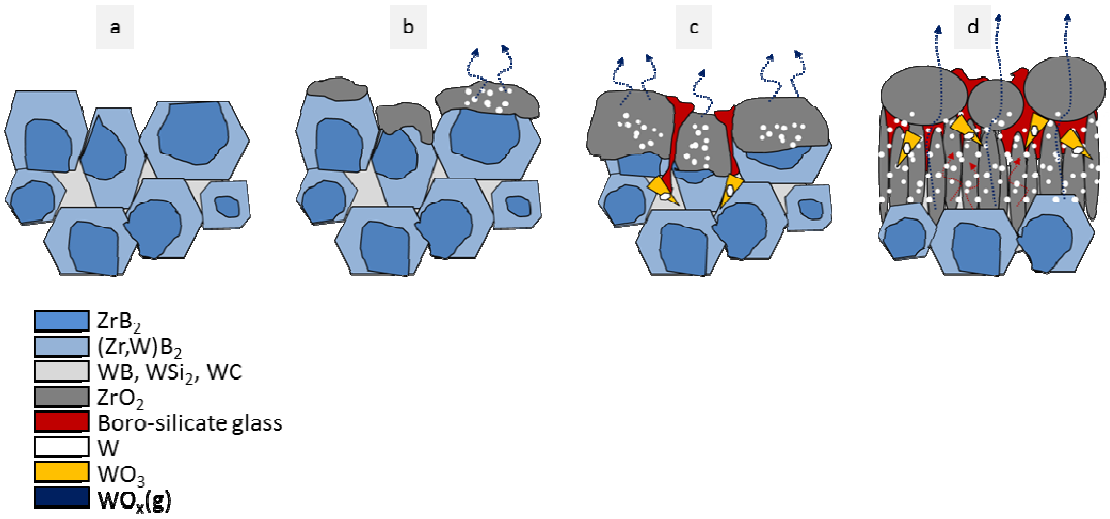

Fig. 13: Sketch of the oxidation phenomena occurring at 1650°C in the W-doped ZrB_2 composite.